Korean J. Chem. Eng., 39(9), 2353-2360 (2022)
DOI: 10.1007/s11814-022-1157-5

pISSN: 0256-1115
eISSN: 1975-7220

An integrated dendrite-free zinc metal electrode for corrosion inhibition in aqueous system

Yi-Fan Hu‡, Li-Feng Zhou‡, He Gong, He Jia, Peng Chen, Yi-Song Wang, Li-Ying Liu, and Tao Du†

Section of Environmental Protection Key Laboratory of Eco-Industry
School of Metallurgy, Northeastern University Liaoning 110819, China
(*Received 2 March 2022 • Revised 12 April 2022 • Accepted 28 April 2022*)

Abstract−Zinc ion batteries have gotten increasing attention as a potential candidate for lithium-ion batteries, due to their high specific capacity (820 $mAh \cdot g^{-1}$), energy density, and safety. Inevitably, dendrite and corrosion create some trouble for this system. Herein, an integrated Zn electrode coated by Zn-Al metal oxides prepared by a simple spin-coating method was utilized to increase the rechargeability for aqueous zinc ion batteries. By coating the Zn anode with an artificial electrolyte interface, the wettability of Zn anodes was improved and impedance was reduced. The coating suppressed not only the appearance of dendrite but also the formation of corrosion products. The symmetrical cells with coating have a low overpotential (43 mV) and an excellent life span. Meanwhile, the applied full batteries exhibit an improved capacity retention rate (86.67% after 120 cycles), great rate performance and low apparent activation energy (24.6 $KJ \cdot mol^{-1}$). The simple production methods and superior corrosion suppression effects provide new ideas for the anode protection of aqueous system batteries.

Keywords: Aqueous System, Zinc Ions Batteries, Anode, Protective Coating, Zn-Al Mixed Metal Oxides

INTRODUCTION

Non-aqueous lithium-ion batteries (LIBs) have dominated the worldwide energy storage industry for the past few decades, due to their high energy density, high power density, and extended cycle life. However, limited lithium supplies, high costs, and safety concerns are limiting their future usage in large-scale energy storage [1-3]. Finding a candidate for LIBs is becoming the focus of research. Zinc ion batteries (ZIBs) have gotten considerable attention as a potential participant, especially aqueous batteries. As the anodes of ZIBs, zinc metal anodes have high specific capacity (820 $mAh \cdot g^{-1}$) and energy density, low redox potential (−0.76 V vs. standard hydrogen electrode), low cost, and safety [4-7]. However, used directly in a neutral or weakly acidic electrolyte, zinc anodes still have some problems such as dendrite, hydrogen evolution reaction, and passivation, which decay capacity, coulombic efficiency and even cycle [8-12].

To overcome the problems, certain techniques, such as Zn/CNT [13], Zn@ZnO [14], three-dimensional zinc foam [15], MOF, ZIF8@Zn [16], MXene@Zn [17], Cu-foam@Zn [18], have been tried. Structure optimization strategies can increase the contact area between electrode and electrolyte, reducing the local current and nucleation overpotential, promoting the uniform deposition of Zn ions and slowing dendrite growth. Meanwhile, it also faces the risk of hydrogen evolution reaction. High-concentration Zn^{2+} electrolyte improves the trouble happening on the surface of the Zn anode effectively [19-23]. However, a high-concentration electrolyte means higher costs, high electrolyte viscosity, and low ion conductivity, which may cause poor discharge capacity at high current density and low power density. Besides, protective coating is recognized as an effective strategy to stabilize Zn anode. Coating materials used in the previous reports include inorganic (ALD-Al_2O_3 [24], kaolin [25], nanao-$CaCO_3$ [26], TiO_2 [27], nano), metal (Au, Ag) [28,29] and poly (vinyl butyral [30], polyamide [42]). Generally, the functional layers should have the following properties: 1) high ionic conductivity and low electronic conductivity; 2) hydrophilic and can exist stably in aqueous media; 3) mechanical stability; and 4) rich in polar groups. With a strong electrostatic attraction to zinc ions and a lower nucleation energy barrier, those coatings can promote uniform zinc ion deposition, reduce corrosion and hydrogen evolution side reactions, and improve cycling stability. For instance, Zhao et al. created a polyamide layer with a unique hydrogen-bonding network and the capacity to firmly coordinate with zinc ions, which can not only harmonize zinc ions migration with uniform nucleation but also inhibit dissolved O_2 and water. The modification strategy takes the advantage of the benefits of simplicity and high cost/time effectiveness, resulting in a high research value and broad application prospects. However, the majority of current studies focus on the materials of coating and performance analysis, while ignoring the effects of coatings on reaction kinetics.

In this paper, we describe a method for preparing a simple integrated electrode that is corrosion-free and can suppress side reactions. The electrode was created by spinning a Zn-Al mixed metal oxide (ZA) onto a zinc foil via a spin coater. The coating can reduce overpotential (43 mV, 55% less than bare zinc) and extend the cycling lifespan effectively. The rate performance and capacity retention of full cell was also improved significantly. Meanwhile, the results of

†To whom correspondence should be addressed.
E-mail: dut@smm.neu.edu.cn
‡These authors make an equal contribution to this work.

optical observations proved that dendrite growth and corrosion reaction can be effectively suppressed on the integrated anode. Furthermore, a complete electrochemical calculation was provided to confirm the positive effects of the coating on reaction kinetics.

EXPERIMENTAL AND METHOD

1. Materials Preparation

Zn-Al mixed metal oxides (ZA) were obtained by calcining the bimetallic hydroxide as the precursor at a certain temperature. The precursor was produced by the co-precipitation method [39]. In brief, 100 ml of 1 mmol $Zn(NO_3)_2$ and 0.5 mmol $Al(NO_3)_3$ were added dropwise to the buffer of Na_2CO_3, and NaOH was used to maintain the solution PH=10 during the dripping process. The precursor solution was placed in a water bath at 85 °C for 4 hours. After cooling to room temperature, the precipitate was filtered out and washed with water and alcohol, then put in a drying oven to dry overnight at 60 °C. Finally, the dried sample was calcined in a muffle furnace at 450 °C for 4 hours; the resulting product was ZA. Similarly, other samples were made in the same way, including the ratio of Zn to Al is 3, 1, 0.5, which were named ZA-3, ZA-2, ZA-1, ZA-0.5. ZA was mixed with Super P and SBS with a weight radio of 8 : 1 : 1 in deionized water and stirred for 4 h. The above slurry was coated on a Zn foil with a diameter of 16 mm by a spin coater at a rate of 4,000 rpm and then dried under a vacuum at 60 °C overnight.

2. Characterization

The scanning electron microscopy (SEM) images of the precursor, ZA were obtained by Quanta250FEG. The dendrites of the symmetrical cell were observed by a high-magnification optical microscope. X-ray diffraction (XRD) patterns were recorded by D8 ADVANCE. Functional group composition was measured by Fourier transform IR(FTIR). The wettability of the electrodes before and after the coating was tested by DSA25. The Brunauer Emmett-Teller (BET) surface area was measured by nitrogen adsorption-desorption using ASAP2460 Micromeritics.

3. Electrochemical Measurements

The objects of electrochemical measurements include Zn-Zn symmetric battery and Zn/MnO_2 full battery. Zn-Zn symmetric cells were assembled with two same zinc foils (bare or ZA coated Zn), glass fibers, button battery case (CR2032) and a 3 M $ZnSO_4$ aqueous electrolyte. The Zn/MnO_2 full battery was constructed with a MnO_2 electrode as the cathode, button battery case, zinc foil (bare or ZA coated Zn) as the anode, a solution of 3 M $ZnSO_4$ and 0.1 M $MnSO_4$ as the electrolyte, and glass fibers as the separator. All galvanostatic charge/discharge was carried out in a voltage range of 0.9-1.8 V on a Landt battery station. Cyclic voltammetry (CV) and electrochemical impedance spectroscopy (EIS) measurements were performed on an electrochemical workstation.

RESULTS AND DISCUSSION

ZA was prepared by calcination of hydrotalcite. After being calcined at 723 K for 4 h, X-ray diffraction (XRD) patterns of the samples are shown in Fig. 1(a). The XRD patterns of the precursor reveal clear hydrotalcite characteristics (JCPDS#48-1023). By contrast, the XRD patterns of the calcined product are typical of the ZnO phase (JCPDS#36-1464), while the peaks of the Al_2O_3 phase are almost invisible, demonstrating that the bimetallic oxide is not a simple mechanical composite of ZnO and Al_2O_3. Al^{3+} is dispersed in the structure of ZnO without the formation of spinel species; a

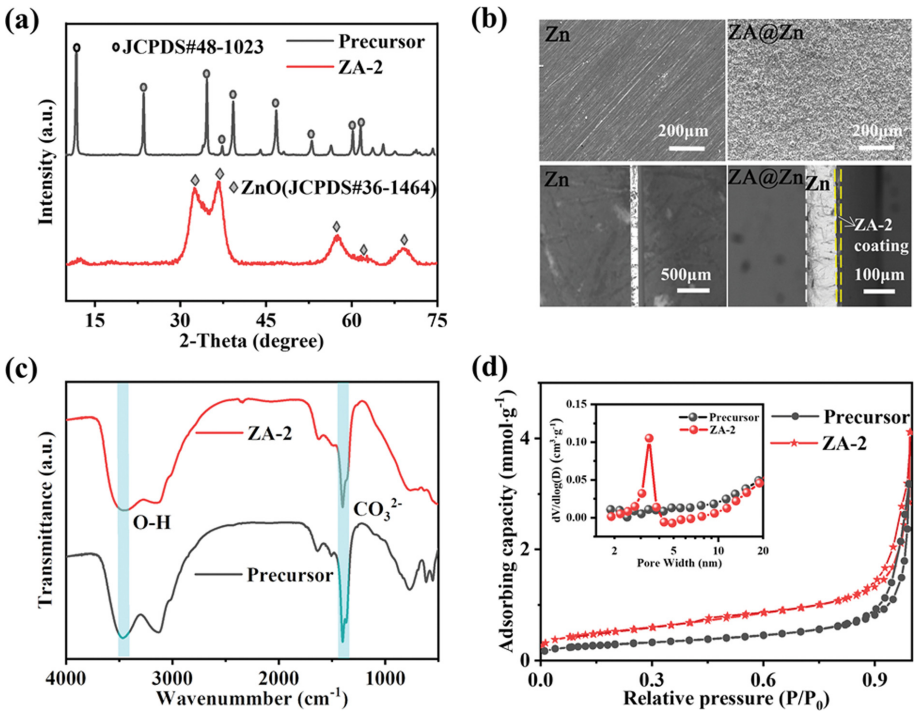

Fig. 1. (a) XRD pattern of bare Zn and ZA-2@Zn; (b) SEM images of bare Zn, ZA-2@Zn plane and cross section; (c) FTIR spectra of ZA-2 and precursor; (d) nitrogen adsorption and desorption curve of the precursor and ZA.

ZnO phase doped with Al^{3+} is formed. The introduction of Al ions can effectively improve the conductivity and stability of the material; it enabled reducing polarization and maintaining the coating stable in cycle [41]. The precursor was converted into mixed metal oxides with a similar structure [31]. Moreover, the intensity of the XRD diffraction peaks changed with the Zn/Al ratio (Fig. S1). Scanning electron microscopic (SEM) images of bare zinc and the ZA-2@Zn plane and cross section are shown in Fig. 1(b). A dense, porous, and uniform protective layer with a thickness of about 16 μm clearly covers the surface of Zn. The magnification of the precursor is shown in Fig. S2. For the images of other ZAs (Fig. S3. S4), the structure of hexagons can still be seen; the ions of Zinc and aluminum are evenly distributed throughout the structure. This is consistent with previous findings, which show that when a precursor is heated, water and CO_2 are released by a cratering mechanism rather than by exfoliation, and the crystal morphology is preserved [32].

The Fourier transform infrared (FT-IR) spectra of ZA and its precursor are shown in Fig. 1(c) and Fig. S5; the intense broadband at approximately 3,500 cm^{-1} is put down to the O-H stretching vibration of the hydroxyl groups attached to Zn and Al. The intensity of O-H decreased after calcination, indicating the dihydroxylation. A stronger and narrower absorption at 1,450 cm^{-1} attributed to carbonates was observed. Similarly, the intensity of carbonates decreased after calcination, which corresponds to carbonate decomposition. At this temperature, undecomposed carbonates could explain the remaining carbonates on the ZA [33]. The absorption peaks in the range of 500-850 cm^{-1} are attributed to M-OH (M is Zn or Al ions) lattice vibrations. After calcination, the number of absorption peaks decreased, indicating that Al ions are disseminated into ZnO crystals. The nitrogen adsorption and desorption curves of the precursor and ZA-2 are shown in Fig. 1(d). Both curves belong to type II and have a hysteresis loop of type H3 [34], implying that the precursor and ZA-2 pore structure is mostly formed of mesoporous. Water and CO_2, as a result of dehydroxylation and interlayer carbonate decomposition, lead to an enlarged specific surface area (from 23.6 to 40.9 m^2 g^{-1}, the specific surface area of other samples is shown in Support Information Table S1). The desorption of CO_2 and H_2O makes sample form a mesoporous structure, providing abundant active adsorption sites. The porous structure of the ZA coating and the binding energy of zinc ions adsorption will reduce the nucleation overpotential of zinc ions, guiding the uniform deposition of zinc ions [43]. And in all ZAs, the specific surface area of ZA-2 is the smallest (Fig. S6, S7, Table S1); it can prevent the accumulation of zinc ions.

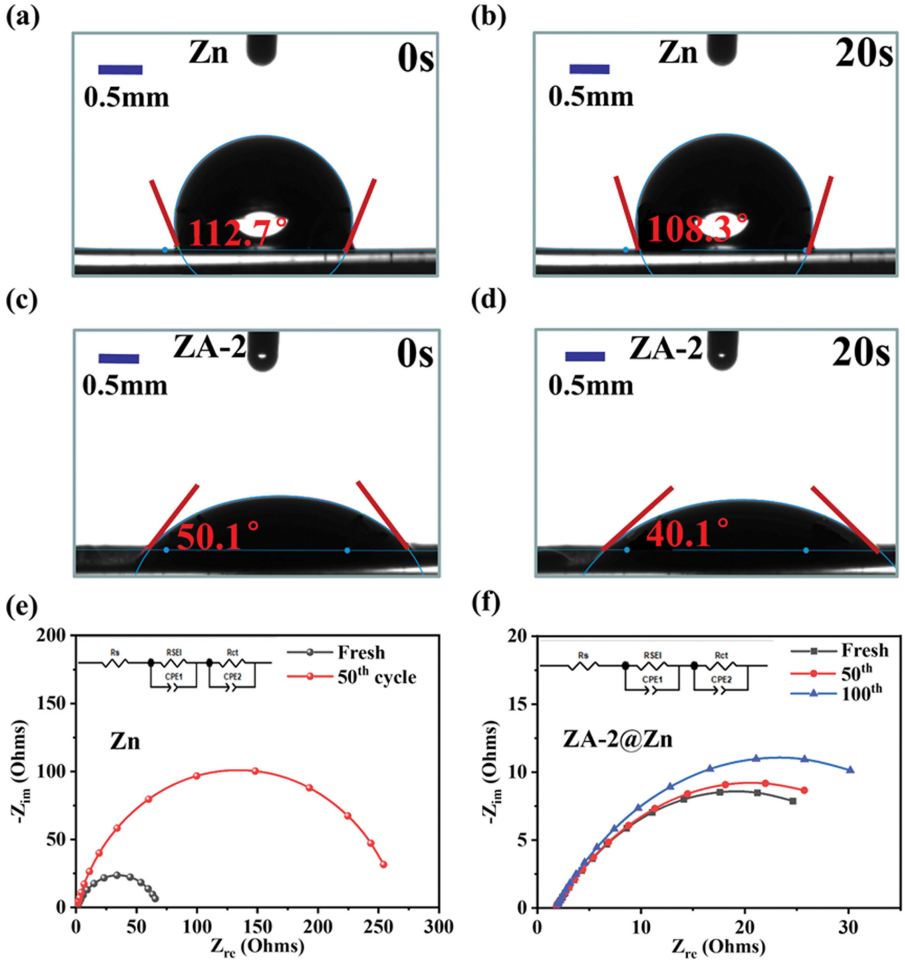

Fig. 2. (a)-(d) Contact angles of Zn and ZA-2@Zn; The EIS of Zn-Zn symmetric with bare Zn anode at the end of the charging process in the fresh and 50th (e), and ZA-2@Zn anode at the end of the changing process in the fresh, 50th, 100th (f).

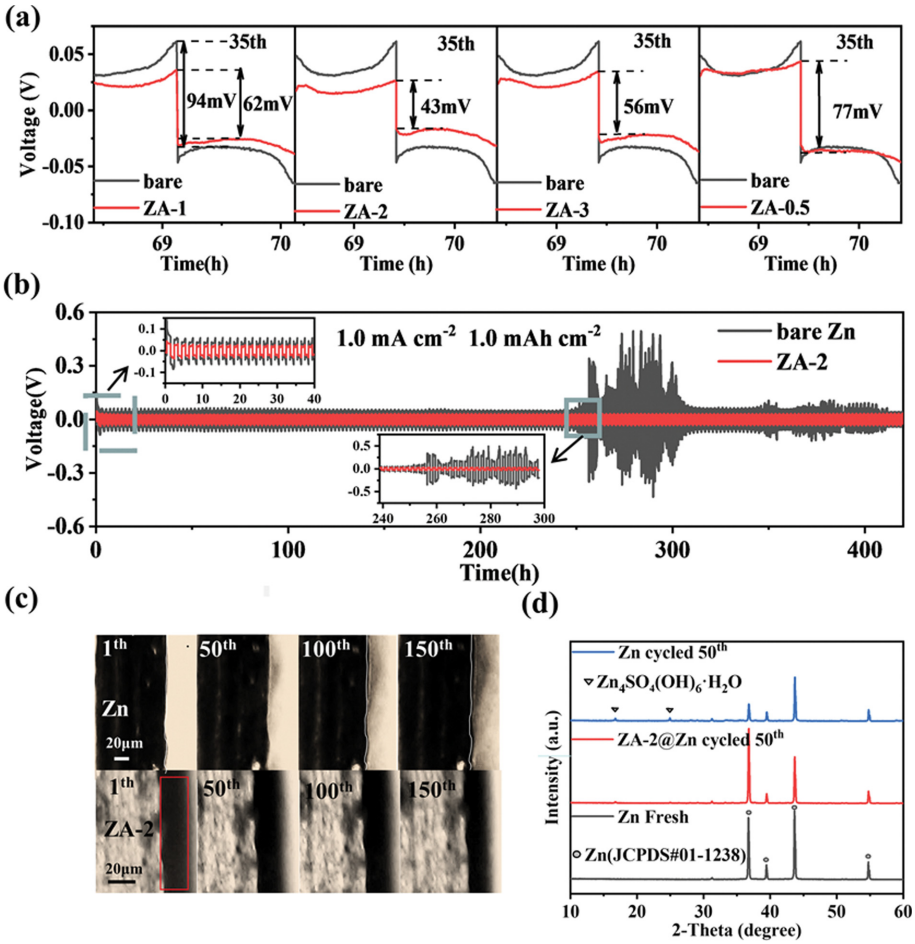

Fig. 3. (a) Charge-discharge profiles of bare Zn and ZA@Zn symmetric cells at 35th; (b) long-term cycling stability of bare Zn and ZA-2@Zn; (c) images of the front surface of bare Zn and ZA-2@Zn in an asymmetric transparent cell after the specified numbers of plating/stripping cycles; (d) The XRD pattern of Zn and ZA-2@Zn before cycling and after 50 cycles.

The wetting angles of Zn and ZA-2@Zn were tested to gain a better understanding of the effect of the ZA-2 coating. The results are depicted in Fig. 2(a)-(d). After 30 seconds, the contact angle between zinc and electrolyte had stabilized at 108.3°. In contrast, ZA-2@Zn has a much smaller contact angle than Zn, which is only 40.1°. It reflects that ZA-2@Zn has higher surface energy, which can effectively improve the electrode's wettability to the electrolyte. The increased wettability makes it easier for zinc ions to enter the Zn surface during the deposition process, which profits zinc ions the transmission and uniform deposition [26]. The electrochemical impedance spectroscopy (EIS) of bare Zn and ZA-2@Zn symmetrical batteries was tested under different cycles to further analyze the protective effect of the ZA-2 coating. The results and the equivalent circuit are shown in Fig. 2(e)-(f), and the fitting results are in good agreement with the experimental data. After 50 cycles of bare zinc, both its R_S and R_{ct} have risen obviously. The change is due to the gradual destruction of the interface structure between the electrode and the electrolyte during the cycle, which will result in the destruction of the electrode and slow the zinc inlay reaction [37]. In comparison, ZA-2@Zn not only has a low impedance value but also can maintain stability during the cycle. It indicates that the ZA-2 coating can inhibit the side reactions between the electrode and the electrolyte, reducing the polarization and impedance of the battery, and enhancing the reaction kinetics of zinc ion plating and stripping [35,36].

The effect of different types of ZA coating on the plating and stripping of zinc ions in a symmetrical battery was investigated, and the results are shown in Fig. 3(a). The current density and capacity were set at 1 mA cm^{-2} and 1 mAh cm^{-2}. All batteries made of ZA-2@Zn have lower polarization than bare zinc. Among them, ZA-2@Zn symmetrical battery exhibits a voltage hysteresis of 43 mV, which campares favorably with most of reporded studies (Table S2, Supporting Information). The overpotential of the symmetric cell was determined by ionic conductively and Zn transference number; the ZA-2 has a excellent ion conductivity and a low electrode impedance, allowing for more Zn transference. The finding indicates that the ZA coating can effectively accelerate ion mobility during zinc ion deposition and stripping the process.

The long-term cycling stability was tested to determine the stability and durability of the coating, and the results are shown in Fig. 3(b) (ZA-1, ZA-3, ZA-0.5 in Fig. S8). Bare Zn exhibits an unstable time and voltage curve that fluctuates violently after 260 h; it is due to a short circuit caused by dendrites formed by the uneven zinc ions deposition puncturing the separator. In comparison, ZA-2@Zn

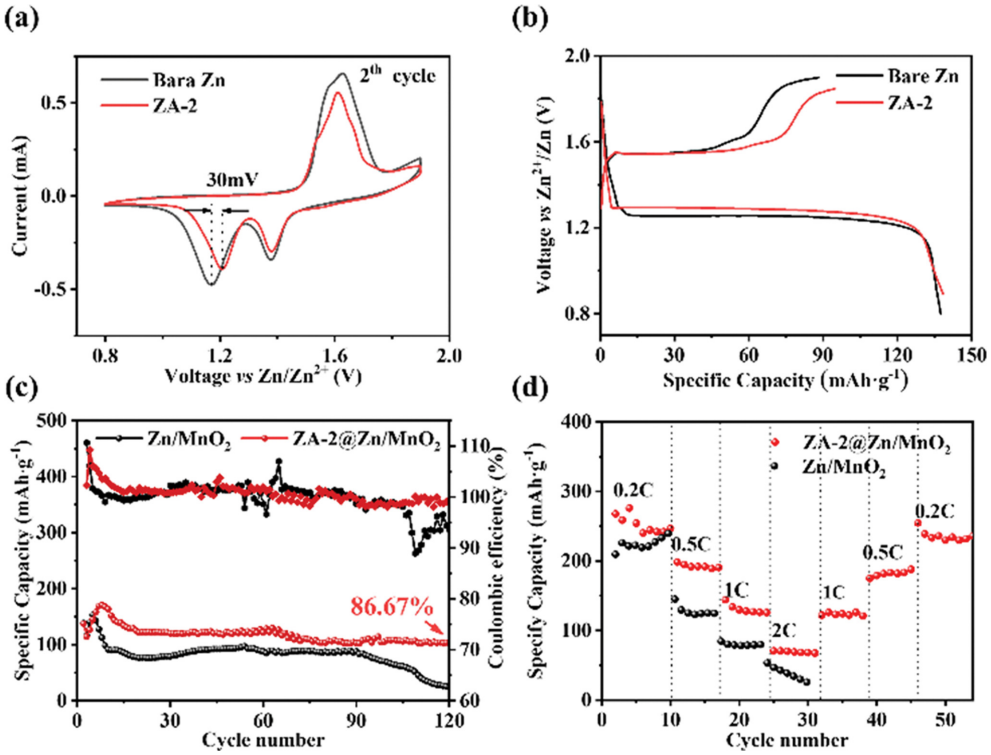

Fig. 4. (a) CV for 2nd cycle of ZA-2@Zn/MnO_2 and Zn/MnO_2 cell; (b) Charge and discharge diagram of the first cycle of both cells; (c) Cycling stability of both cells at 1C; (d) rate capacity of the Zn/MnO_2 and ZA-2@Zn/MnO_2 cell ranging from 0.2C to 2C.

not only has a lower voltage hysteresis but better stability, remaining stable after 450 h without voltage fluctuation or short circuit. It means that the coating can guide the uniform deposition of zinc ions during charge and discharge and is long-term stable in the electrolye. In the rate test of the symmetrical battery (Fig. S9), the stability of ZA-2@Zn was further proved. Under different current densities, ZA coatings all exhibit lower voltage hysteresis and can remain stable after an excessive current density test.

Corrosion product is a major reason for ZIBs short-circuiting. A transparent visualization battery of Zn and ZA-2@Zn was used to observe corrosion product and dendrite growth at a current density of 4 mA cm^{-2} to further explore the protective effect of ZA-2 coating, and the results are shown in Fig. 3(c). It can be observed in the Zn-Zn symmetric battery that small dendritic protrusions and loose corrosion products begin to appear on the smooth zinc surface when the number of cycles reaches 50. The protrusions gradually grow larger and accumulate as the number of cycles increases. After cycling 150 times, a layer of corrosion products is formed on the surface of the bare zinc. In contrast, the surface of ZA-2@Zn can remain smooth and free of visible corrosion products. It proves that ZA coating can reduce direct contact between the electrolyte and zinc electrode, thereby slowing the occurrence of side reactions. The XRD pattern of the electrode after 50 cycles confirms it as well in Fig. 3(d). The pattern of bare zinc after 50 cycles shows obvious characteristic peaks at 18° and 27°, which correspond to corrosion product ($Zn_4SO_4(OH)_6{\cdot}H_2O$), indicating that the bare zinc has obvious corrosion during the cycle [37]. It was further proved that the ZA-2 coating can reduce water activity and water-induced side reactions, guide the uniform deposition of zinc ions, and improve cycle stability.

To evaluate the application of ZA@Zn in a practical scenario, full cells paired with a MnO_2 cathode were assembled (the theoretical capacity of MnO_2 is 308 mAh·g^{-1}). CV was used to investigate the redox reactions and the reversibility of bare Zn/MnO_2 and ZA-2@Zn/MnO_2 cells for the initial three cycles during the charge and discharge process. As shown in Fig. S10, two cathodic peaks at 1.38 and 1.16 V appear in the CV curve of Zn/MnO_2, which can be attributed to the two-step reduction reaction from Mn^{4+} to Mn^{3+} to Mn^{2+}. Relatively, an asymmetric anode peak consisting of two sub-peaks at 1.58 and 1.62 V is observed, which corresponds to two reverse oxidation reactions. Similar peaks are seen in ZA-2@Zn at 1.21 V/1.38 V and 1.61 V/1.51 V. It means that the coating will not change the redox reaction in the battery.

The second circle of the two CV curves is compared in Fig. 4(a). Clearly, the ZA-2@Zn/MnO_2 battery has a lower voltage polarization (30 mV) than the Zn/MnO_2 battery, indicating its excellent reversibility due to the ZA-2 coating protection [39]. The corresponding charge-discharge curves of Zn/MnO_2 and ZA-2@Zn/MnO_2 are shown in Fig. 4(b), indicating that those two batteries delivered similar redox reactions as well. Fig. 5(c) shows the cycling performance of Zn/MnO_2 and ZA-2@Zn/MnO_2 at 1C (200 mA·g^{-1}). ZA-2@Zn/MnO_2 cell displays much better cycling stability than Zn/MnO_2. The discharge capacity of Zn/MnO_2 gradually decreases after a short period of increase as the cycle increases and stabilizes at around 95 mAh·g^{-1}. After 80 cycles, the capacity rapidly decays and only has a capacity of 25 mAh·g^{-1} at 120 cycles. In

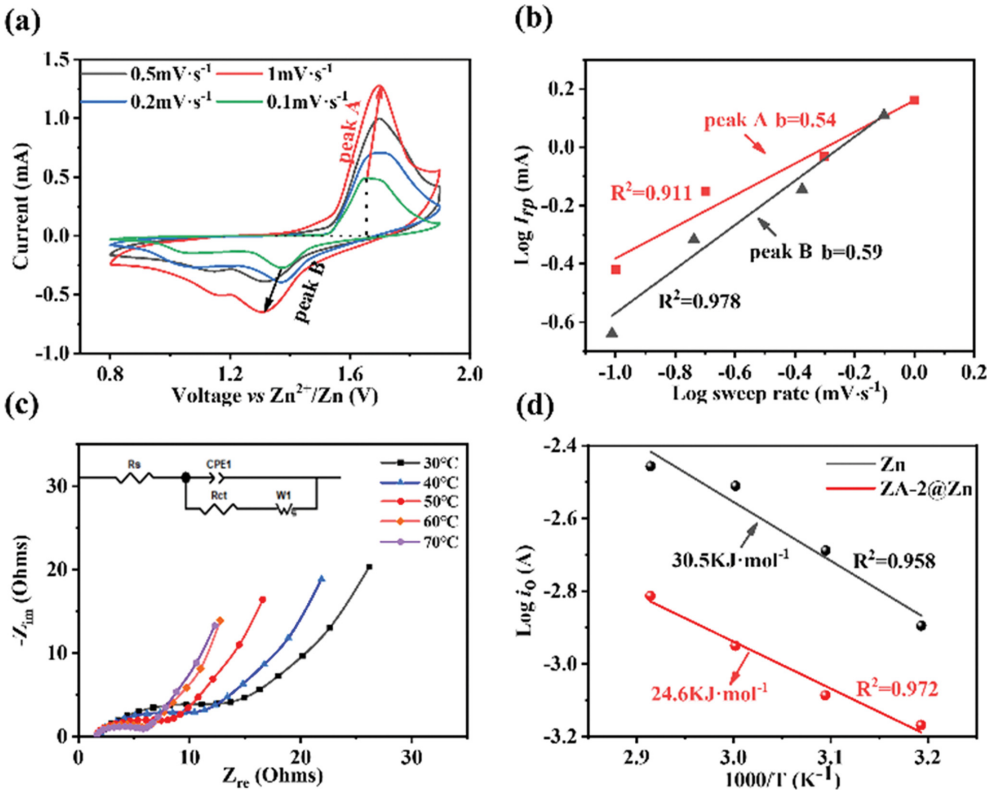

Fig. 5. (a) CVs at different scan rates for ZA-2@Zn/MnO_2; (b) Relationship between the peak current and scan rata in logarithmic format; (c) The EIS of ZA-2@Zn/MnO_2 at different temperatures; (d) Arrhenius plots of log i vs. T^{-1} for the Zn/MnO_2 and ZA-2@Zn/MnO_2 electrodes. The lines are the linear fitting results.

contrast, ZA-2@Zn/MnO_2 exhibits a discharge capacity of 136 mAh·g^{-1}, and maintains a discharge capacity of 103.5 mAh·g^{-1}, with a high capacity retention of 87.64% after 120 cycles. The higher changing capacity and capacity retention rate of the ZA-2@Zn-MnO_2 cell could be attributed to the inhibition of corrosion, side reactions and the maintenance of a homogeneous interface via the ZA-2 coating, which works as a high-performance artificial SEI layer. Furthermore, the coulombic efficiency of the battery has been significantly improved. The charge-discharge profiles in the 1st, 15th, 50th, 100th cycle of the bare Zn/MnO_2 and ZA-2@Zn/MnO_2 are shown in Fig. S11; ZA-2@Zn/MnO_2 has a much smaller polarization than Zn/MnO_2. The result indicates that the ZA-2 coating can effectively improve cycle stability and reduce electrode polarization during the charge and discharge process.

Fig. 4(d) and Fig. S13 show the rate capability of bare Zn/MnO_2 and ZA-2@Zn/MnO_2 battery, and the corresponding charge-discharge curves at each current density are shown in Fig. S12. As clearly seen from Fig. 4(d), ZA-2@Zn/MnO_2 shows a more superior rate capability than bare Zn/MnO_2 at all the current densities. At a discharging rate of 0.2C, the specific capacity of the ZA-2@Zn/MnO_2 battery was about 250 mAh·g^{-1}. Even after going through the charge and discharge process of a 3C rate, the specific capacitance of ZA-2@Zn/MnO_2 can still reach 246 mAh·g^{-1}. In comparison, the Zn/MnO_2 battery not only exhibits lower capacity at various densities but also has short-circuited at the current density of 5C (Fig. S13). The result reveals that the ZA-2@Zn/MnO_2 battery has excellent rate performance.

The diffusion coefficient of zinc ions was analyzed and calculated by measuring the cyclic voltammetry (CV) curve at different scan rates (0.1-1 mV s^{-1}) to further understand the reaction kinetics of ZA-2@Zn/MnO_2, and the results are shown in Fig. 5(a). The oxidation peak in the curve goes to a higher potential as the scan rate increases, while the reduction peak moves to a lower point as the scan rate increases. An empirical power-law connection exists between the measured current (i) and sweep rates (v):

$$i=av^b$$

where i is current, v is the scan rata, and a and b are the variables that may be changed, The slope of log(i) vs. log(v) b determines the b value, which gives into the charge storage mechanism: a b value of 0.5 implies a diffusion-controlled process, whereas 1.0 indicates a surface capacitive-controlled process. By plotting log(i) vs. log(v) (Fig. 5(b)), the b values of peaks A and B are calculated to be 0.54 and 0.59, respectively. This means that the corresponding redox reactions in the ZA-2@Zn/MnO_2 electrode are mainly diffusion-controlled activities [38].

The apparent activation energies of the two electrodes were estimated from the electrochemical impedance spectra to further examine the kinetics of the electrode materials. The activation energy (E_a) reflects the energy necessary for electrode interfacial film and change-transfer: (1) Electron injection and extraction between current collector and zinc anode; (2) Desolvation and exfoliation of

ions at the anode interface. The entire redox process exhibits a close dependence on temperature, which was verified by EIS measurements [40]. Fig. 5(c) shows the Nyquist plots of the electrodes at various temperatures. The equivalent circuit model was used to fit the experimental data, as shown in the insets in Fig. 5(d). The activation energies of ZA-2@Zn/MnO_2 and Zn/MnO_2 are determined to be 24.6 and 30.5 KJ mol^{-1} (E_a=−RKIn10, K is the slope of the fitting line in Fig. 5(d)). The diffusion apparent activation energy (E_{aD}) corresponds to the process of stripping of zinc ions from the zinc anode; it can be computed using the following formula: E_{aD}=−RKIn10 (K is the slope of the fitting line in Fig. S14, S15) from the line of Log D and T^{-1}. The apparent activation energy of diffusion is 15.3 and 22.18 KJ·mol^{-1}, respectively. The battery with a lower surface activation energy can perform better electrochemically, effectively avoid HER caused by free water in the solvation sheath, and speed up the reaction kinetics.

CONCLUSION

The simple integrated electrode with ZA coating can effectively reduce electrode polarization (43 mV, 91% less than bare Zn), inhibit the formation of corrosion products, and prolong the lifespan of symmetric cells. The introduction of ZA coating improves electrode wettability, it reduces impedance and the binding energy of zinc ions adsorption, which accelerates the reaction kinetics and guides the uniform deposition of zinc ions. Meanwhile, ZA-2@Zn/MnO_2 batteries exhibit a great capacity retention rate (86.67% after 120 cycles), superior rate performance, and a low apparent activation energy (24.6 KJ·mol^{-1}). Moreover, the simple manufacturing methods and superior corrosion suppression effects provide new ideas for aqueous system battery anode protection.

ACKNOWLEDGEMENTS

Y. Hu and L. Zhou make an equal contribution to this work. We acknowledge funding for Key R&D Plan of Liaoning Province (2021JH2/10300003 & 2020JH2/10300103) and the Natural Science Grant of China (No. 22078054). Special thanks to China Scholarship Council (CSC).

CREDIT AUTHORSHIP CONTRIBUTION STATEMENT

Y. Hu: Design experiment, Data collection, Writing - original draft. L. Zhou: Design experiment, review & editing. H. Gong, P. Chen, Y. Wang, H. Jia and L. Liu: Discussion, review and editing. T. Du: Supervision. Supervision, Funding, Writing - review & editing.

SUPPORTING INFORMATION

Additional information as noted in the text. This information is available via the Internet at http://www.springer.com/chemistry/journal/11814.

REFERENCES

1. J. M. Tarascon and M. Armand, *Nature*, **15**, 356 (2001).
2. M. Li, J. Lu, Z. Chen and K. Amine, *Adv. Mater.*, **30**, 1800561 (2018).
3. D. Larcher and J. M. Tarascon, *Nat. Chem.*, **7**, 19 (2015).
4. G. G. Yadav, D. Turney, J. Huang, X. Wei and S. Banerjee, *ACS Energy Lett.*, **4**, 2144 (2019).
5. T. Xiong, Z. G. Yu, H. Wu, Y. Du, Q. Xie and J. Chen, *Adv. Energy Mater.*, **9**, 1803815 (2019).
6. D. Chao, W. Zhou and C. Ye, *Angew. Chem. Int. Ed.*, **3**, 7823 (2019).
7. F. Wang, E. Hu, W. Sun, T. Gao, X. Ji, X. Fan, F. Han, X. Q. Yang, K. Xu and C. Wang, *Energ. Environ. Sci.*, **11**, 3168 (2018).
8. B. Tang, L. Shan, S. Liang and J. Zhou, *Energ. Environ. Sci.*, **12**, 3288 (2019).
9. V. Yufit, F. Tariq, D. S. Eastwood, M. Biton, B. Wu, P. D. Lee and N. P. Brandon, *Joule*, **3**, 485 (2019).
10. Y. Zuo, K. Wang, P. Pei and P. Zhang, *Mater. Today Energy*, **20**, 100692 (2021).
11. S. Higashi, S. W. Lee, J. S. Lee, K. Takechi and Y. Cui, *Nat. Commun.*, **7**, 11801 (2016).
12. Q. Yang, G. Liang, Y. Guo, Z. Liu, B. Yan, D. Wang, Z. Huang, X. Li, J. Fan and C. Zhi, *Adv. Mater.*, **31**, 1903778 (2019).
13. C. Zheng, V. Augustyn, J. Wen, Y. Zhang, M. Shen, B. Dunn and Y. Lu, *Adv. Mater.*, **23**, 791 (2011).
14. X. Xie, S. Liang, J. Gao, S. Guo, J. Guo and C. Wang, *Energ. Environ. Sci.*, **13**, 503 (2020).
15. M. Chamoun, B. J. Hertzberg, T. Gupta, D. Davies, S. Bhadra, B. Van Tassell, C. Erdonmez and D. A. Steingart, *Npg, Asia Mater.*, **7**, 178 (2015).
16. X. Pu, B. Jiang, X. Wang, W. Liu and C. Xu, *Nano-Micro Lett.*, **12**, 15 (2020).
17. Y Qian, C. Wei, Y Tian, B. Xi and Y. Qian, *Chem. Eng. J.*, **7575**, 129685 (2021).
18. C. Li, X. Shi, X Ma, M. Han and S. Liang, *Chem. Eng. J.*, **379**, 122248 (2019).
19. N. Zhang, F. Cheng and Y. Liu, *Am. Chem.*, **138**, 12894 (2016).
20. W. Fei, O. Borodin, G. Tao, X Fan and C. Wang, *Nat. Mater.*, **17**, 543 (2018).
21. J. Zhao, J. Zhang, W. Yang, B. Chen, Z. Zhao, H. Qiu, S. Dong, X. Zhou, G. Cui, L. Cui and L. Chen, *Nano Energy*, **57**, 625 (2019).
22. Q. Zhang, Y. Ma, Y. Lu, L. Li, F. Wan, K. Zhang and J. Chen, *Nat. Commun.*, **11**, 4460 (2020).
23. C. Bai, H. Jin, Z. Gong, X. Liu and Z. Yuan, *Energy Storage Mater.*, **28**, 247 (2020).
24. H. He, H. Tong, X. Song and J. Liu, *J. Mater. Chem. A*, **8**, 7836 (2020).
25. C. Deng, X. Xie, J. Han, T. Yan and S. Liang, *Adv. Funct. Mater.*, **30**, 2000599 (2020).
26. L. Kang, M. Cui, F. Jiang, Y. Gao and C. Zhi, *Adv. Energy Mater.*, **8**, 1801090 (2018).
27. K. Zhao, C. Wang, Y. Yu, M. Yan, Q. Wei, P. He, Y. Dong, Z. Zhang, X. Wang and L. Mai, *Adv. Mater. Interfaces*, **5**, 1800848 (2018).
28. Q. Lu, C. Liu, Y. Du, X. Wang and D. Mikhailova, *ACS Appl. Mater. Inter.*, **13**, 16868 (2021).
29. M. Cui, Y. Xiao, L. Kang, W. Du, Y. Gao, X. Sun, Y. Zhou, X. Li, H. Li, F. Jiang and C. Zhi, *ACS Appl. Energy Mater.*, **2**, 6490 (2019).
30. J. Hao, X. Li, S. Zhang, F. Yang, X. Zeng, S. Zhang, G. Bo, C. Wang and Z. Guo, *Adv. Funct. Mater.*, **30**, 2001263 (2020).

31. G. Starukh, Rozovik, O. Oranska and O. Organo, *Nanoscale Res. Lett.*, **11**, 228 (2016).
32. P. Mustrowski, L. Chmielarz, E. Bozek, M. Sawalha and F. Roessner, *Mater. Res. Bull.*, **39**, 263 (2004).
33. F. Cavani, F. Trifirò and A. Vaccari, *Catal. Today*, **11**, 173 (1991).
34. J. W. Boclair and P. S. Braterman, *Chem. Mater.*, **11**, 303 (1999).
35. A. C. Kozen, C. Lin, A. J. Pearse, M. A. Schroeder, X. Han, L. Hu, S. Lee, G. W. Rubloff and M. Noked, *ACS Nano*, **9**, 5884 (2015).
36. E. Kazyak, K. N. Wood and N. P. Dasgupta, *Chem. Mater.*, **27**, 6457 (2015).
37. L. Yan, X. Zeng, Z. Li, X. Meng, D. Wei, T. Liu, M. Ling, Z. Lin and C. Liang, *Mater. Today Energy*, **13**, 323 (2019).
38. C Chen, Z. Wang and B. Zhang, *Energy Storage Mater.*, **8**, 161 (2017).
39. L. Qiu, W. Chen and B. Qu, *Polym. Degrad. Stabil.*, **87**, 433 (2005).
40. X. Xie, S. Liang, J. Gao, S. Guo, J. Guo, C. Wang, G. Xu, X. Wu, G. Chen and J. Zhou, *Energy Environ. Sci.*, **13**, 503 (2020).
41. Z. C. Jin, I. Hamberg and C. G. Granqvist, *J. Appl. Phys.*, **64**, 5117 (1988).
42. Z. Zhao, J. Zhao, Z. Hu, J. Li, J. Li, Y. Zhang, C. Wang and G. Cui, *Energy Environ. Sci.*, **12**, 1938 (2019).
43. A. R. Mainar, E. Iruin, L. C. Colmenares, A. Kvasha, I. de Meatza, M. Bengoechea, O. Leonet, I. Boyano, Z. Zhang, J. A. Blazquez, *J. Energy Storage*, **15**, 304 (2018).

Supporting Information

An integrated dendrite-free zinc metal electrode for corrosion inhibition in aqueous system

Yi-Fan Hu, Li-Feng Zhou, He Gong, He Jia, Peng Chen, Yi-Song Wang, Li-Ying Liu, and Tao Du†

Section of Environmental Protection Key Laboratory of Eco-Industry
School of Metallurgy, Northeastern University Liaoning 110819, China
(*Received 2 March 2022 • Revised 12 April 2022 • Accepted 28 April 2022*)

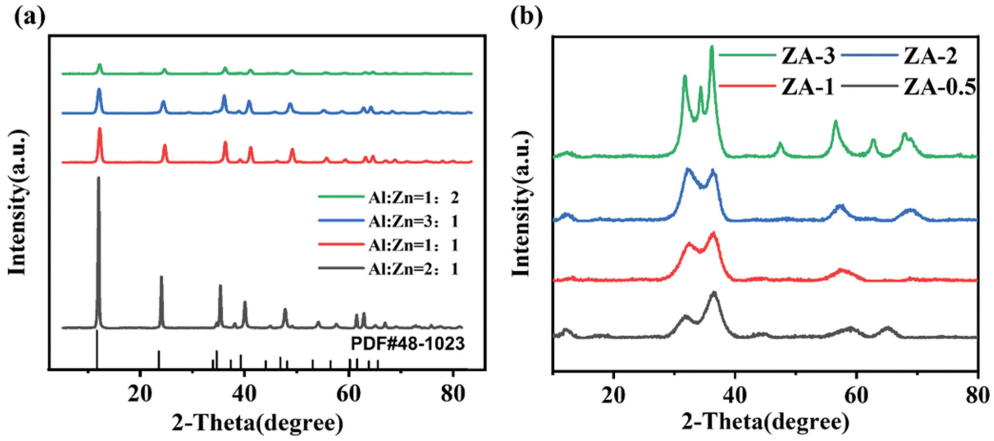

Fig. S1. XRD patterns of (a) the Precursor and (b) ZA.

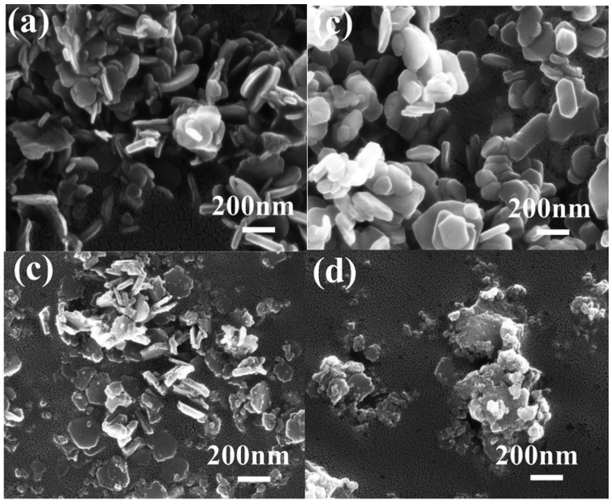

Fig. S2. SEM images of the Precursor, the radio of Zn and Al is (a) 3, (b) 2, (c) 1, (d) 0.5.

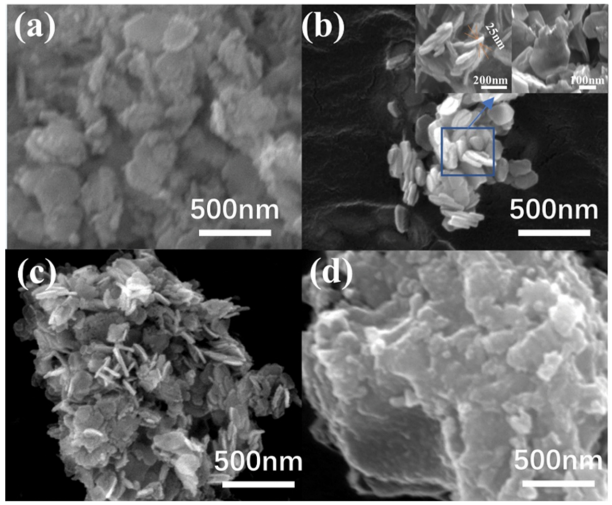

Fig. S3. SEM images of the ZA, the radio of Zn and Al ions is (a) 3, (b) 2, (c) 1, (d) 0.5.

Experimental

Cathode electrode production: MnO_2 was synthesized by a hydrothermal method. 6 mmol $KMnO_4$ and 1 mmol $MnSO_4{\cdot}H_2O$ were dissolved in 70 mL distilled water under stirring 30 min. The precursor solution was transferred into a Teflon contained autoclave with a volume of 100 mL and then heated at 180 °C for 12 h. After cooling to room temperature, the black precipitate was vacuum filtered until the PH reached 7 and then dried at 100 °C in

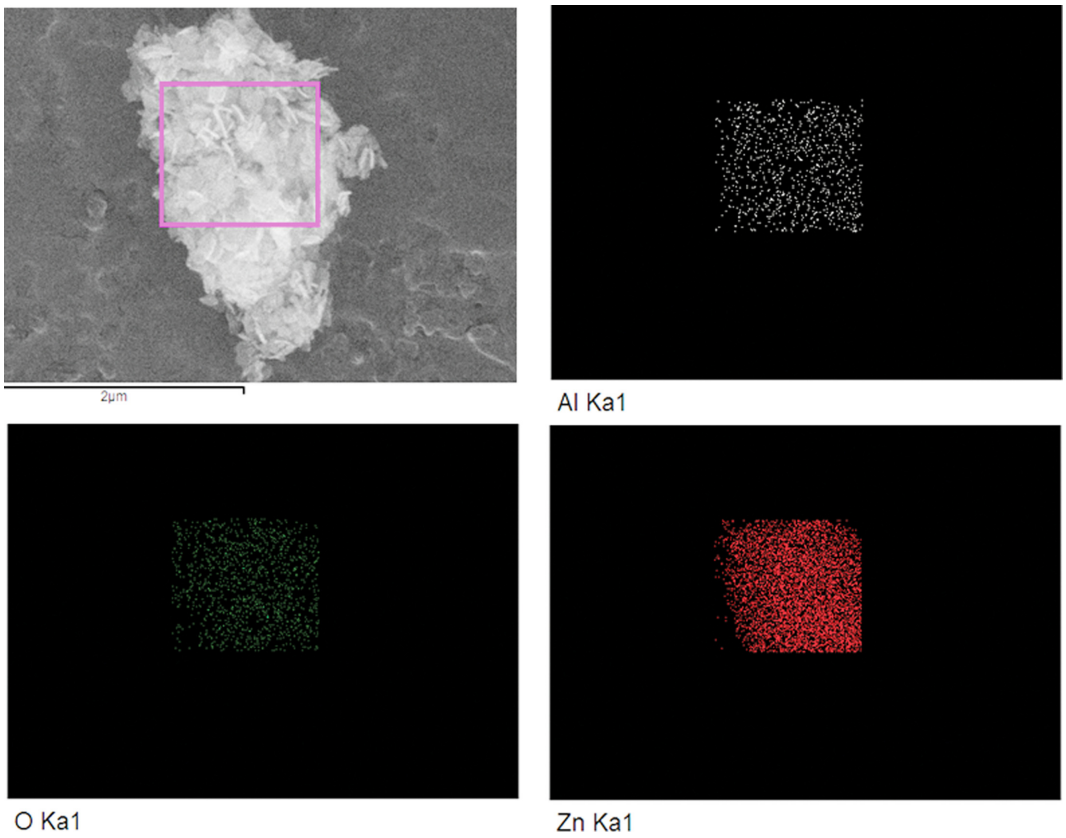

Fig. S4. EDS images of the ZA-2.

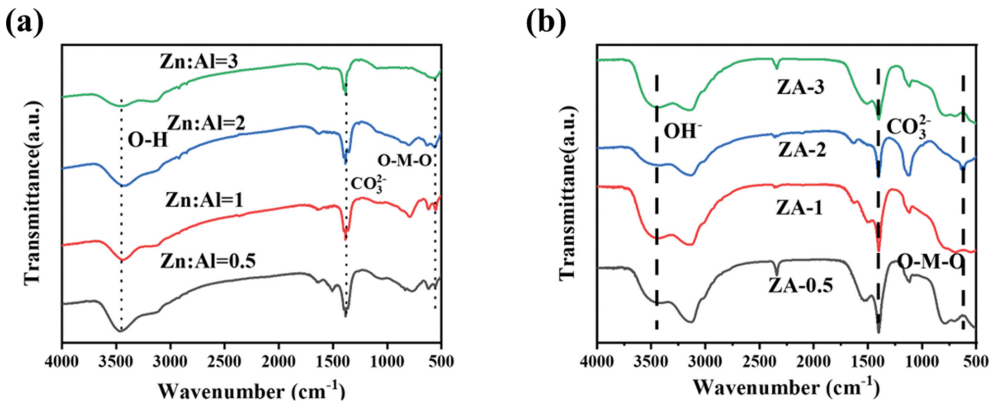

Fig. S5. FTIR spectra of (a) the Precursor and (b) ZA.

air overnight.

MnO_2 was mixed with Super P and polyvinyl difluoride (PVDF) with a weigh radio of 7 : 2 : 1 in NMP and stirred for 6 h. The stirred slurry is coated on the stainless steel foil and placed in a vacuum drying oven at 80 °C to dry overnight. Finally, the stainless steel foil is cut into a disc with a diameter of 12 mm as the cathode electrode. The mass loading of MnO_2 was around 1.4 mg on each disk.

Table S1. The specific surface area of ZAs

Sample	ZA-3	ZA-2	ZA-1	ZA-0.5
Specific surface area ($m^2 \cdot g^{-1}$)	59.2349	41.9820	124.0438	189.7033

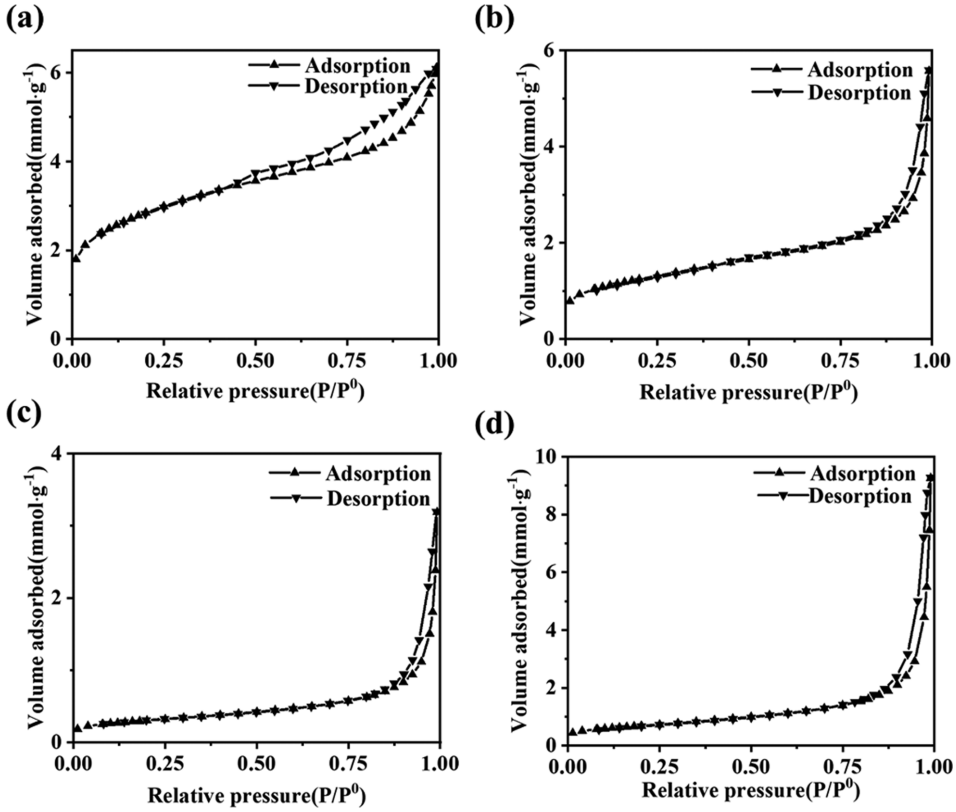

Fig. S6. Nitrogen adsorption and desorption of the Precursor (the radio of Zn and Al ions is (a) 0.5, (b) 1, (c) 2, (d) 3).

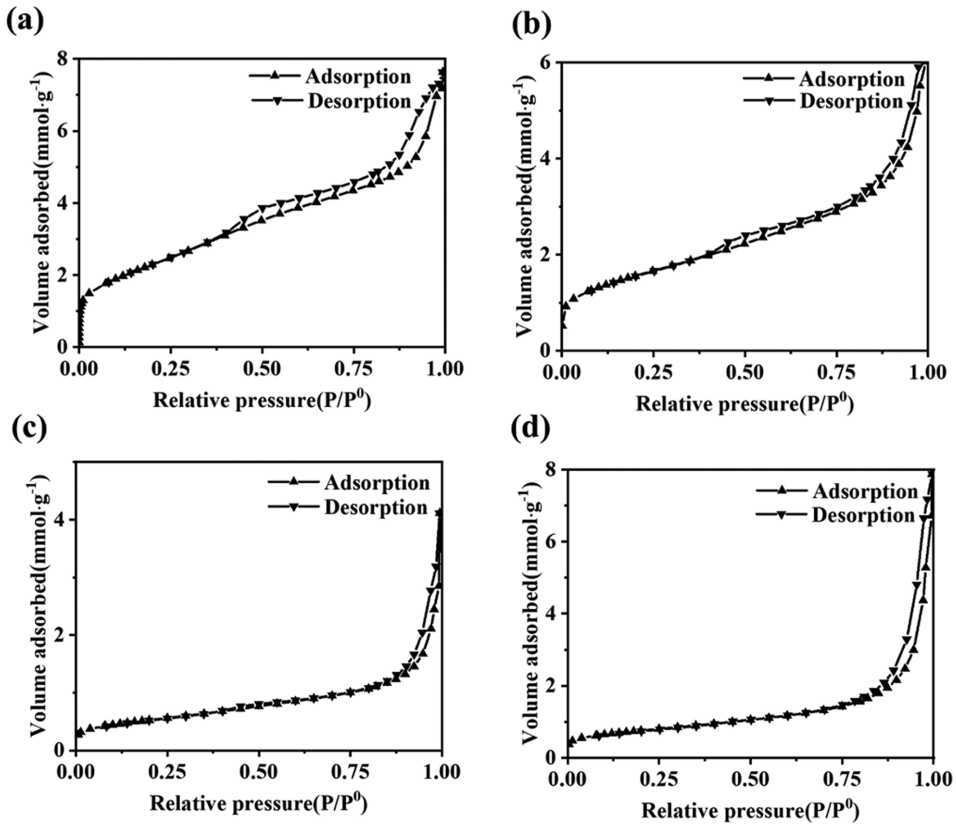

Fig. S7. Nitrogen adsorption and desorption of ZA (the radio of Zn and Al ions is (a) 0.5, (b) 1, (c) 2, (d) 3).

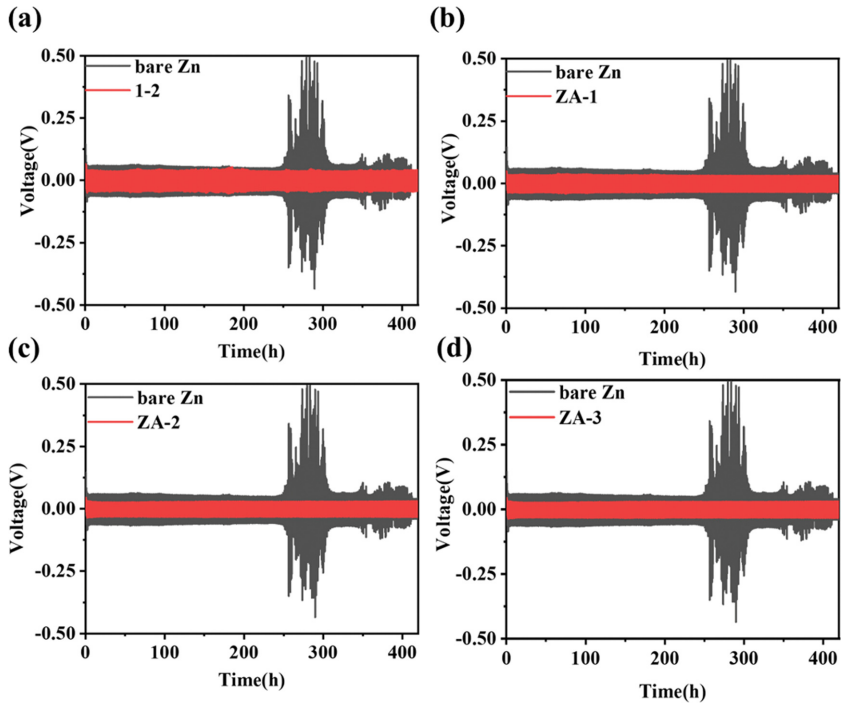

Fig. S8. Long-term cycling stability of bare Zn and ZA symmetrical battery. (a) ZA-1/2, (b) ZA-1, (c) ZA-2, (d) ZA-3.

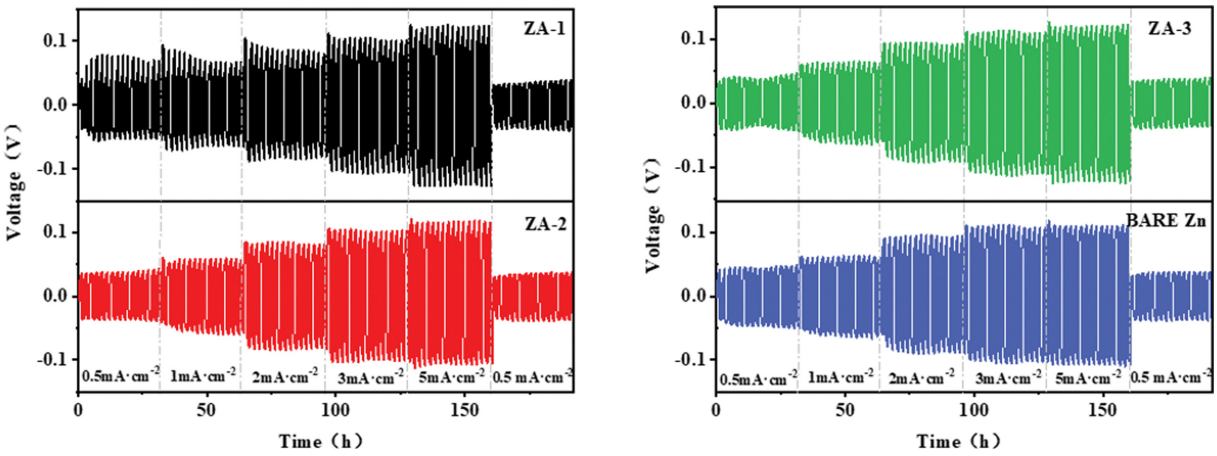

Fig. S9. Rates test of bare Zn and ZA symmetrical battery.

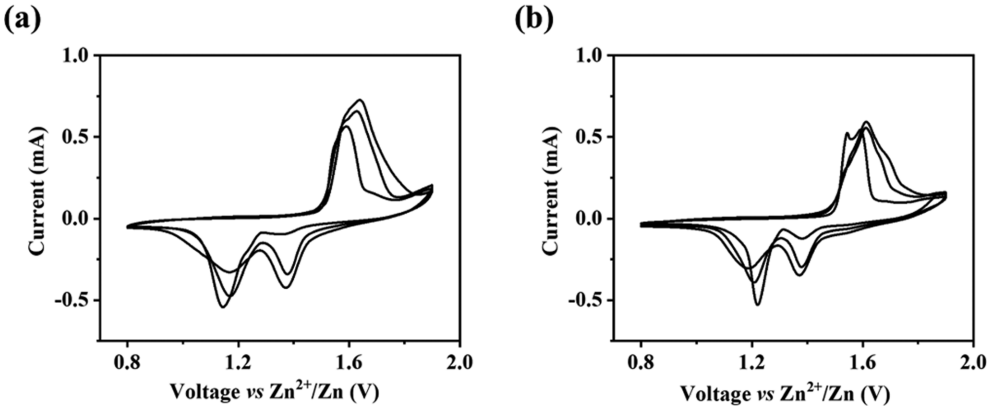

Fig. S10. CV of (a) Zn/MnO_2 and (b) ZA-2@Zn/MnO_2 full cell.

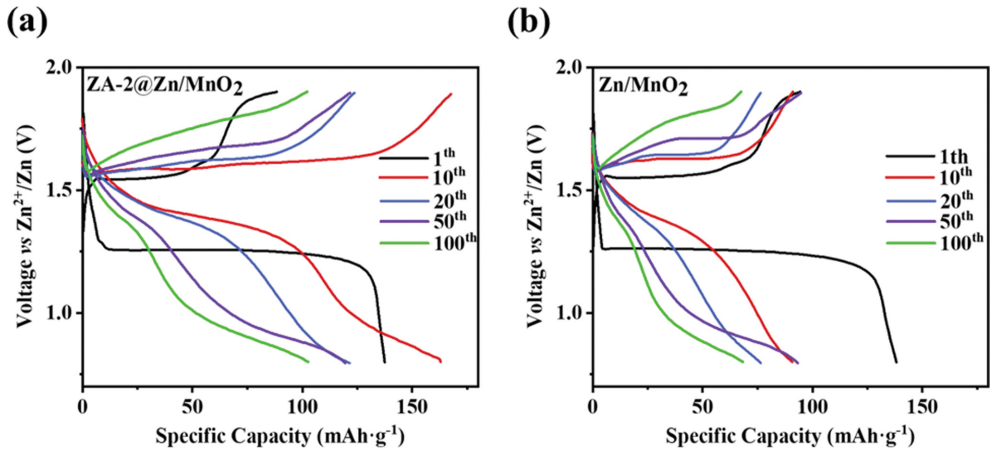

Fig. S11. The charge-discharge profiles in the 1, 15, 50, 100 cycles of (a) the bare Zn/MnO_2 and (b) ZA-2@Zn/MnO_2.

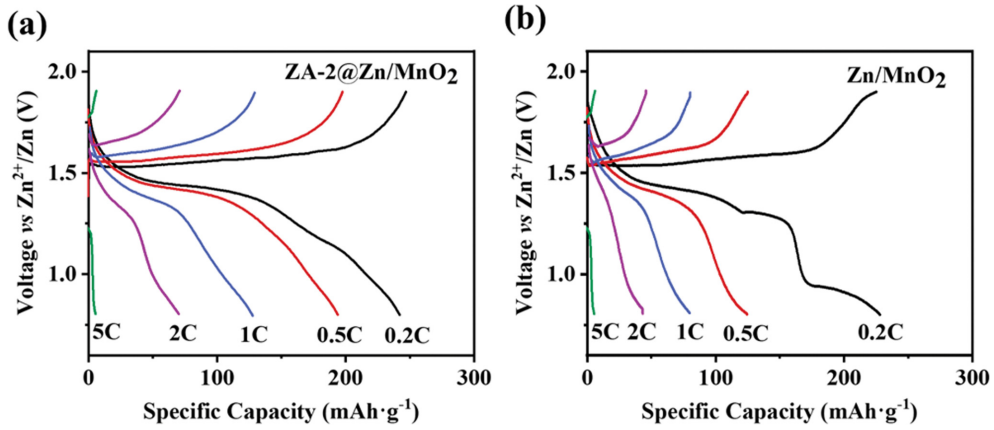

Fig. S12. The charge-discharge profiles of (a) Zn/MnO_2 and (b) ZA-2@Zn/MnO_2 at each current density.

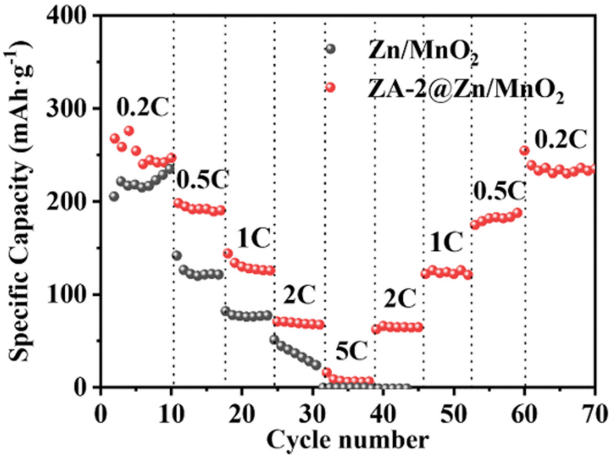

Fig. S13. Rate capacity of the Zn/MnO_2 and ZA-2@Zn/MnO_2 cell ranging from 0.2C to 5C.

Electrochemical Characterization

The impedance curves show one condensed semicircle in the medium-frequency region, which could be assigned to the reaction resistance, and an inclined line in the low-frequency range, which could be considered Warburg impedance. R_s is the effective resistance due to electrolyte impedance and electrical contacts and is obtained from the intercept of the semicircle at high frequency with the x-axis. W is the Warburg impedance seen as a sloping line in the low-frequency regime, which is associated with Zn^{2+} ions diffusion in the bulk of the electrode. The mid-frequency semicircle is fitted with a depressed semicircle, corresponding to (R_{ct}|| CPE1), where CPE1 is constant phase elements, which can be attributed to the complex charge transfer processes from the electrolyte to the electrode material. It is suggested that R_{ct} refers to the charge transfer resistance. The exchange current (i_0) and the apparent activation energy (E_a) for the zinc intercalated into the active materials can be calculated from Eq. (1) 2 and the Arrhenius equation, Eq. (2) 2, respectively.

$$i_o = RT/nFR_{ct} \quad (1)$$

$$i_o = A\exp(-E_a/RT) \quad (2)$$

where A is a temperature-independent coefficient, R is the gas constant, T(K) is the absolute temperature, n is the number of transferred electrons, and F is the Faraday constant.

The EIS can also be used to calculate the zinc diffusion coefficient using the following Eq. (3).

$$D = R^2T^2/2A^2n^4F^4C^2\sigma^2 \quad (3)$$

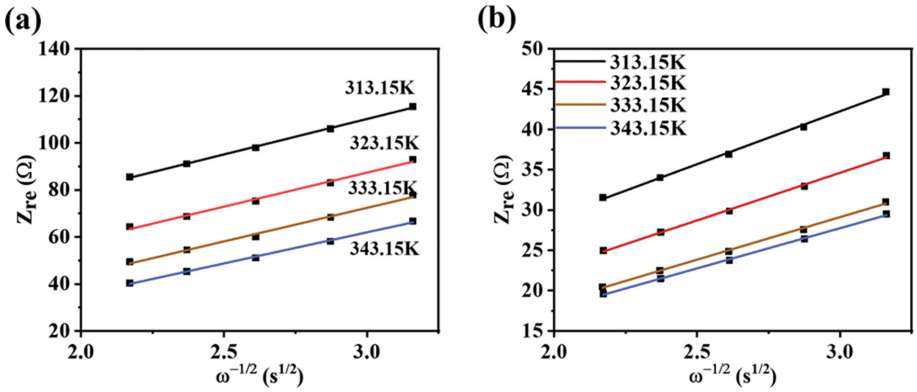

Fig. S14. Real parts of the complex impedance versus $w^{1/2}$ at different temperatures of (a) Zn-MnO_2 and (b) ZA-2@Zn-MnO_2.

Table S2. Caparison on the electrochemical properties of ZA-2@Zn anode and the previously reported Zn anode

Electrode	Current density (mA cm^{-2})	Capacity (mAh cm^{-2})	Voltage hysteresis (mV)	Life	Referemce
ZA@Zn	**1**	**1**	**43**	**>560**	**This work**
ZnO array	1	1	78	400	[1]
Al_2O_3	1	1	36.5	500	[2]
TiO_2	1	1	114	150	[3]
ZnS	2	2	70	1,100	[4]
MXene	5	1	108	100	[5]
$CaCO_3$ coated	0.25	0.05	104	836	[6]
Kolin layer	4.4	1.1	140	800	[7]
Polyamide	10	10	160	150	[8]
Nano. ZnO	5	1.25	84	500	[9]

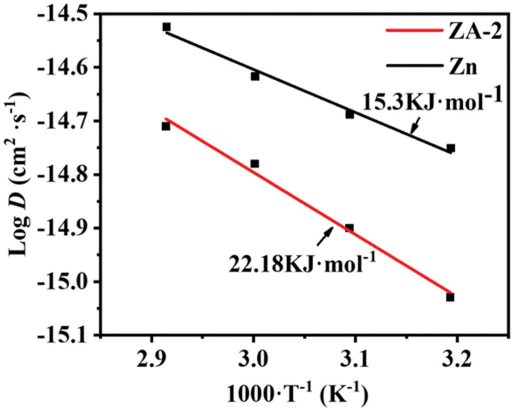

Fig. S15. Log D versus T^{-1} plot during zinc insertion.

where R is the gas constant, T is the absolute temperature, A is the surface area of the cathode, n is the number of electrons transferred in the half-reaction for the redox couple, which is equal to 2, F is the Faraday constant, C is the concentration of Zn ions in the solid (0.1099 mol·cm^{-3}), D is the diffusion coefficient (cm^2 s^{-1}), and σ is the Warburg factor, which is relative to Z_{re}. σ can be obtained from the slope of the lines in Fig. S10.

$$Z_{re}=R_s+R_{ct}+\sigma\omega^{-1/2} \quad (4)$$

REFERENCES

1. H. He, H. Tong, X. Song and J. Liu, *J. Mater. Chem. A.*, **8**, 7836 (2020).
2. K. Zhao, C. Wang, Y. Yu, M. Yan, Q. Wei, P. He, Y. Dong, Z. Zhang, X. Wang and L. Mai, *Adv. Mater. Interfaces* **5**, 1800848 (2018).
3. J. Hao, B. Li, X. Li, X. Zeng, S. Zhang, F. Yang, S. Liu, D. Li, C. Wu and Z. Guo, *Adv. Mater.*, **32**, 2003021 (2020).
4. N. Zhang, S. Huang, Z. Yuan, J. Zhu, Z. Zhao and Z. Niu, *Angew. Chem. Int. Ed.*, **60**, 2861 (2020).
5. L. Kang, M. Cui, F. Jiang, Y. Gao and C. Zhi, *Adv. Energy Mater.*, **8**, 1801090 (2018).
6. C. Deng, X. Xie, J. Han, T. Yan and S. Liang, *Adv. Funct. Mater.*, **30**, 2000599 (2020).
7. Z. Zhao, J. Zhao, Z. Hu, J. Li, J. Li, Y. Zhang, C. Wang and G. Cui, *Energy Environ. Sci.*, **12**, 1938 (2019).
8. Z. Cai, Y. Ou, J. Wang, R. Xiao, L. Fu, Z. Yuan, R. Zhan and Y. Sun, *Energy Storage Mater.*, **27**, 205 (2020).
9. Z. Zhao, J. Zhao, Z. Hu, J. Li, J. Li, Y. Zhang, C. Wang and G. Cui, *Energy Environ. Sci.*, **12**, 1938 (2019).